RSC Advances

PAPER

View Article Online
View Journal | View Issue

Cite this: *RSC Adv.*, 2021, **11**, 37923

Facile preparation of high loading filled PVDF/$BaTiO_3$ piezoelectric composites for selective laser sintering 3D printing†

Shiping Song, Yijun Li, Qi Wang and Chuhong Zhang *

Received 15th September 2021
Accepted 15th November 2021

DOI: 10.1039/d1ra06915b

rsc.li/rsc-advances

3D printed piezoelectric devices, due to their sufficient multidimensional deformation and excellent piezoelectric properties, are one of the most promising research directions. However, the lack of high loaded piezoelectric composites is the key bottleneck restricting the enhancement of the piezoelectric output. In this work, we successfully prepared a novel high loaded polyvinylidene fluoride (PVDF)/barium titanate ($BaTiO_3$) piezoelectric composite suitable for selective laser sintering (SLS) 3D printing *via* solid state shear milling (S^3M) technology. The 50 wt% $BaTiO_3$ filling made the most outstanding contribution to the piezoelectric properties of the composites. The 3D printed cymbal parts with a stress amplification effect exhibited outstanding piezoelectric conversion efficiency and responsiveness, whose open circuit voltage and short circuit current could reach 20 V and 1.1 μA, respectively. This work not only contributed a new high loaded piezoelectric composite for SLS processing, but also provided a novel piezoelectric performance enhancement strategy by the construction of 3D structure.

1. Introduction

With the rapid technological and economic development of our societies, an intelligent industry centered on new materials and new equipments is gradually rising all around the world.[1,2] Due to the ability to realize the mutual conversion of mechanical energy and electrical energy,[3–5] piezoelectric materials have aroused great interest in practical applications, and are widely used in sensing, energy storage, electronics and other fields.[6,7] For example, Li *et al.*[8] demonstrated a non-lead (ZnO) piezoelectric device powered by heart movement. Cheng *et al.*[9] reported a self-powered PVDF sensor for blood pressure monitoring. However, restricted by conventional processing technology, piezoelectric materials are usually only manufactured into two-dimensional (2D) thin films or sheets,[10] whose normal space cannot be fully utilized to produce sufficient deformation, resulting in a limited stress-to-electricity conversion efficiency.[11] Compared with 2D parts, the modulus and deformation of three-dimensional (3D) parts can be adjusted by introducing arrays,[12] holes,[13] lattices[14] and other structures, so as to effectively compensate for the lack of normal deformation in traditional piezoelectric devices and enhance the piezoelectric output.[15] 3D printed piezoelectric devices have received extensive attention due to their high-efficiency stress-to-electricity conversion and have been recognized as one of the most promising research fields.[16]

The composition of materials has a crucial influence on the final performance of 3D printed parts.[17] Nowadays, piezoelectric polymer materials, *e.g.* polyvinylidene fluoride (PVDF)[18] and nylon 11 (PA11),[19] have the advantages of good flexibility, low density and excellent processability.[20] But such polymers cannot satisfy the needs of practical applications due to their low piezoelectric strain constant and conversion efficiency.[21] Piezoelectric ceramics, featuring high piezoelectric constant, figure of merit, Curie temperature and stability, are currently the most applied piezoelectric materials,[22] such as lead zirconate titanate (PZT), barium titanate ($BaTiO_3$), *etc.*[23,24] Therefore, piezoelectric composite materials marrying both the advantages of piezoelectric polymers and piezoelectric ceramics are highly desired for a more satisfactory performance in 3D printing technology.[25]

The filling amount of piezoelectric ceramics is the key factor that determines the piezoelectric properties of the materials. Qi *et al.*[26] reported that 80 wt% $BaTiO_3$ composited with PA11 could exhibit excellent piezoelectric properties. Chamankar *et al.*[27] prepared a PVDF/PZT high loaded composite with improved piezoelectric properties. More and more researchers in the piezoelectric field are focusing on increasing the filling amount of piezoelectric ceramics. However, the common preparation methods of piezoelectric composites mainly employ approaches such as melt blending and solution methods.[28] The obtained composite materials usually exhibit improved processing properties and piezoelectric performances, but because of the polarity difference between the polymer and ceramic,[29] there still

State Key Laboratory of Polymer Materials Engineering, Polymer Research Institute, Sichuan University, Chengdu, 610065, China. E-mail: chuhong.zhang@scu.edu.cn

† Electronic supplementary information (ESI) available. See DOI: 10.1039/d1ra06915b

remain three main problems: (1) poor interface compatibility, (2) low content filling and (3) severe agglomeration of ceramics.[30] In view of the above technical bottleneck, the filling amount of piezoelectric ceramics in the matrix is mostly less than 30 wt%, hindering the further improvement of the piezoelectric performances. The pursuit of a clean and efficient method for the preparation of high filling piezoelectric composites is practically imperative.

Solid state shear milling (S^3M) is a facile technology for processing polymers and modifying organic/inorganic interfaces, based on the principle of polymer mechanochemistry and its unique three-dimensional scissoring structure learning from traditional Chinese stone mills.[31] During S^3M treatments, a large number of shear unit cells can be formed by two milling pans with relative motion and embedded grooves, and the shape and volume of these shear unit cells change periodically.[32] With strong pressure, it seems that many 3D scissors continuously cut the materials, and this enables the grinding and dispersion of the materials at room temperature.[33] Therefore, S^3M equipment can effectively eliminate the agglomeration between ceramic particles and improve the interface compatibility,[34] which has great advantages in the large-scale preparation of polymer-based piezoelectric composite powder with high content filling.

As an important 3D printing technology, selective laser sintering (SLS) can design and construct 3D complex structures by layer-by-layer processing of powder materials.[35] The technical advantages of SLS mainly lie in the ability to manufacture parts with a unique geometric creativity and enhance design flexibility without any expensive additional tools,[36] and it does not involve the rheology and interface compatibility issue of the composites. So SLS might be the most suitable 3D printing technology for processing high loaded piezoelectric composites. It is expected that the 3D piezoelectric parts prepared by SLS can take full advantage of the piezoelectric coefficients in multiple directions and thus boost the piezoelectric properties.[37]

PVDF is a typical piezoelectric polymer material, and exhibits excellent flexibility and processability.[38] As a semi-crystalline and polymorphous polymer, PVDF comprises α, β, γ, δ and ε crystal phases with distinct chain conformations, among which the β crystal, consisting of repetitive TTTT conformation units, exhibits the best piezoelectric properties.[39,40] Therefore, high β phase amount is the key to obtain excellent stress-to-electricity conversion efficiency. $BaTiO_3$ is a widely applied lead-free piezoelectric ceramic material due to its high electromechanical coupling coefficient and piezoelectric constant. However, it is hard, brittle and intolerant to mechanical impact, which greatly limits its piezoelectric applications.[41] People have made great efforts in addressing these issues; for instance, Yang *et al.*[42] reported a flexible piezoelectric pressure sensor based on a polydopamine-modified $BaTiO_3$/PVDF composite film for human motion monitoring. The 17 wt% PDA@BTO/PVDF sensor exhibited a remarkable piezoelectric output voltage of 9.3 V. Jiang *et al.*[43] prepared a flexible piezoelectric pressure tactile sensor based on $BaTiO_3$/PVDF composites by the electrospinning technique, which displayed excellent flexibility and a linear response to external mechanical force. Yang *et al.*[24] introduced PVDF/$BaTiO_3$/CNT piezoelectric energy harvesters with bionic balsa wood structures prepared by 3D printing and supercritical carbon dioxide foaming. The open circuit voltage and short circuit current could reach 19.3 V and 415 nA, respectively.

Herein, we for the first time report a new PVDF/$BaTiO_3$ piezoelectric composite with a high content filling and uniform distribution by S^3M technology and its piezoelectric application in SLS 3D printing. A series of one-piece cymbal parts with excellent piezoelectric properties and responsiveness were designed and manufactured. Three issues were addressed: (1) the dispersion morphology of the composites, (2) the crystallization behaviors of PVDF in SLS and (3) the enhancement mechanism of the piezoelectric properties generated by the cymbal parts. This work not only provides a new type of piezoelectric composite suitable for SLS, but also exhibits great guiding significance for the structural design of 3D piezoelectric parts during SLS processing.

2. Experimental

2.1 Materials

PVDF (FR906, $T_m = 170$ °C, $\rho = 1.77$ g cm^{-3}) was provided by Shanghai 3F New Material Technology Co., Ltd., China. $BaTiO_3$ ($\rho = 6.08$ g cm^{-3}, average particle size = 500 nm) was supplied by Shandong Sinocera Functional Material Co., Ltd., China. The fumed silica (average particle size = 12 nm) was purchased from Evonik, Germany.

2.2 Preparation of the PVDF/$BaTiO_3$ composite powder and the selective laser sintering process

A schematic illustration of the preparation and SLS processing of the PVDF/$BaTiO_3$ nanocomposites is shown in Fig. 1. Initially, PVDF pellets with 25 wt%, 50 wt% or 75 wt% $BaTiO_3$ were milled together in a S^3M reactor for 15 cycles respectively, ensuring that $BaTiO_3$ could be uniformly dispersed in the PVDF matrix. Secondly, the milled powder was extruded by a single-screw extruder (RM-200C, Harbin Harp Electrical Technology Co., Ltd., China). The processing temperature range was 180–220 °C and the rotation rate of the screw was set to 50 rpm. Then, after cryogenic grinding, drying and sieving, the PVDF/$BaTiO_3$ nanocomposite powder suitable for SLS was successfully prepared. The addition of fumed silica was conducive to improving the flowability of the composite powder. The construction process of 3D parts was carried out on SLS equipment (HT 251P, Hunan Farsoon High-Tech Co., Ltd., China). The preheating temperature of the powder was set to 157 °C, the laser power was 15 W and the laser scan spacing was 0.3 mm. According to the difference in $BaTiO_3$ content, the composite powder and corresponding SLS parts were designated as BT25, BT50 and BT75.

2.3 Characterization

2.3.1 The morphology and processability characterizations. The powder morphologies were observed by scanning electron microscopy (SEM, JSM 5900LV, JEOL Co., Ltd., Tokyo,

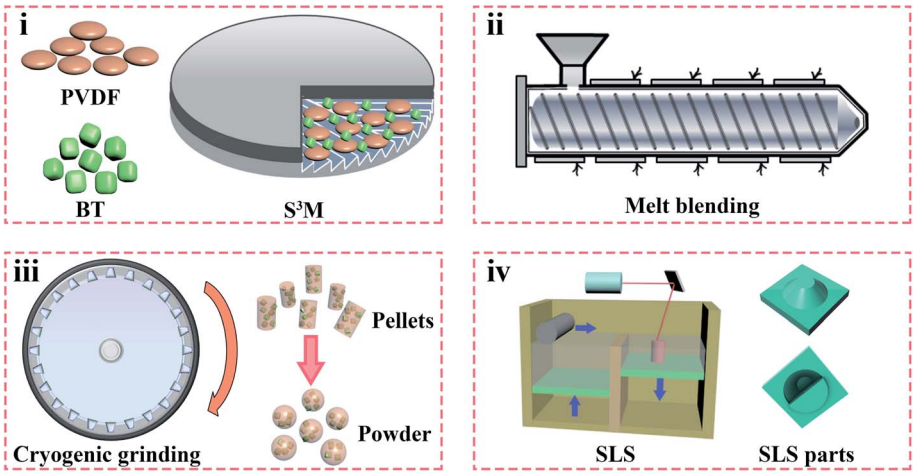

Fig. 1 A schematic illustration of the process for the preparation and SLS processing of the PVDF/$BaTiO_3$ composites.

Japan). The geometric parameters of the powder were tested on a laser diffraction particle size analyzer (Microtrac S3500, Machik Instruments Co., Ltd., USA). The flowabilities of the composite powder were analyzed on a powder rheometer (FT4, Freeman Technology Co., Ltd., UK).

2.3.2 The crystallinity characterizations. The thermal behaviors were studied by a differential scanning calorimeter (DSC, TA-Q20, TA Instruments Co., Ltd., USA). The heating and cooling temperature rates were set to 10 °C min^{-1} and the temperature change range was 40–220 °C. The crystallinity could be calculated using the following equation:[44]

$$X_c = \Delta H_m/(1 - \varphi)\Delta H_m^0 \times 100\% \quad (1)$$

where ΔH_m is the melting enthalpy of the sample, ΔH_m^0 is the melting enthalpy of 100% crystalline PVDF, and φ is the mass fraction of $BaTiO_3$. The analyses of the crystal structures were carried out on a Fourier transform infrared (FT-IR) spectrometer (Nicolet 6700, Thermo Scientific Company, USA). The β phase relative amount of the samples could be calculated using the following equation:[45]

$$F(\beta) = A_\beta/[(K_\beta/K_\alpha)A_\alpha + A_\beta] \quad (2)$$

where A_α and A_β are the absorbance at 760 cm^{-1} and 840 cm^{-1}, respectively, and K_α and K_β are the absorption coefficient at 760 cm^{-1} and 840 cm^{-1}, respectively ($K_\alpha = 6.1 \times 10^4$ cm^2 mol^{-1} and $K_\beta = 7.7 \times 10^4$ cm^2 mol^{-1}).

2.3.3 The piezoelectric characterizations. Before testing, the samples were coated with silver paste on the upper and lower surfaces, respectively, and left for 24 h until the solvent volatilized completely. Then, two uniform silver electrodes were formed on the surface of the piezoelectric parts. The dielectric properties were analyzed by a dielectric impedance spectrometer (Concept 50, Novocontrol, Germany). The test frequency range was set from 100 Hz to 10 MHz. The poling process of the samples was performed by applying an electric field of 3 kV mm^{-1} in a constant temperature oil bath of 90 °C for 30 min. The samples were placed in a Petri dish for 24 h before piezoelectric testing. The piezoelectric properties were studied by a piezoelectric testing system, which mainly included a linear motor (HS01-37 × 166, NTI AG, USA) and an electrometer (6514, Keithley, USA).

3. Results and discussion

3.1 The processability of the PVDF/$BaTiO_3$ composite powder

In order to achieve the uniform dispersion of $BaTiO_3$ and good piezoelectric properties of the composites, nearly spherical tetragonal $BaTiO_3$ particles (Fig. 2(a)) with an average particle size of 500 nm were selected as the piezoelectric reinforcement phase. SEM images of a composite powder prepared by solid state shear milling (S^3M) and cryogenic grinding technology are shown in Fig. 2(b). Due to the strong shear force of the S^3M equipment, the $BaTiO_3$ particles were evenly dispersed in the PVDF matrix without agglomeration, which was extremely beneficial to the improvement of the piezoelectric performance. In addition, the prepared composite powder had an irregular block shape and a rough surface, which was conducive to forming a dense powder bed and fully absorbing the laser during SLS processing. SLS processing also had certain requirements regarding the particle size of the powder. A small particle size of the powder could easily cause electrostatic adsorption and agglomeration. While if the particle size was too large, it was difficult to obtain high dimensional deviation of the SLS parts. Therefore, the average particle size of the SLS powder should be in the range of 20–80 μm and the particle size distribution should be in the range of 1–200 μm. As shown in Fig. 2(c), the average particle sizes of PVDF and the PVDF/$BaTiO_3$ powder were in the range of 40–60 μm and D90 was always less than 150 μm, meeting the requirements of SLS processing. The shear test results are shown in Fig. 2(d) and Table 1. The cohesion (C) and unconfined yield strength (σ_c) of $BaTiO_3$ were 1.82 kPa and 8.48 kPa, respectively, confirming the

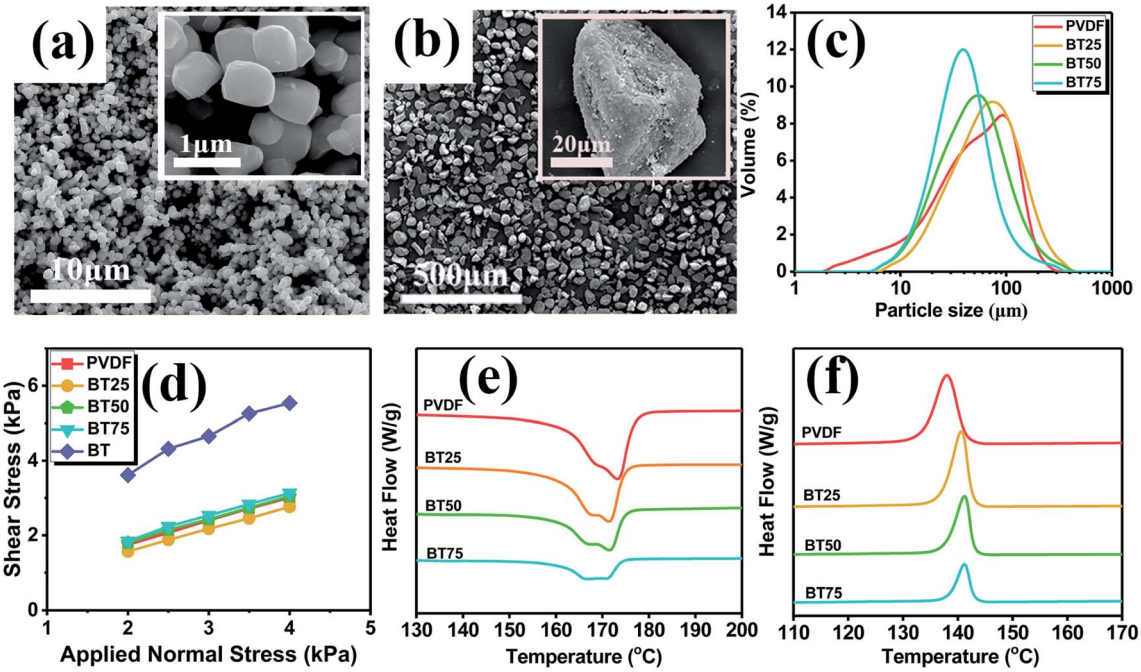

Fig. 2 SEM images of (a) $BaTiO_3$ and (b) BT50 powder. (c) The particle size distribution curves of PVDF and PVDF/$BaTiO_3$ powder. (d) The shear test curves of PVDF, $BaTiO_3$ and PVDF/$BaTiO_3$ powder. The DSC thermograms of the powder: (e) the heating process and (f) the cooling process.

Table 1 Shear properties of the PVDF, PVDF/$BaTiO_3$ and $BaTiO_3$ powder

Sample	C, kPa	σ_c, kPa	ff	φ_i, °	ε, g ml^{-1}
PVDF	0.484	1.76	6.13	32.4	0.795
BT25	0.384	1.35	7.82	30.7	0.954
BT50	0.582	2.09	5.12	31.7	1.17
BT75	0.616	2.24	4.52	32.7	1.35
$BaTiO_3$	1.82	8.48	1.75	43.6	1.14

large cohesive force between the $BaTiO_3$ powder particles. The flow function (ff) of $BaTiO_3$ was only 1.75, representing an extremely viscous flow, so $BaTiO_3$ was a kind of powder particle with poor flowability. Therefore, the cohesion and unconfined yield strength of the composite powder gradually increased with the increase of the $BaTiO_3$ content. This was due to the fact that the addition of $BaTiO_3$ degraded the initial flowability of the powder. The flow functions were all between 4 and 10, representing viscous flow, confirming that PVDF had a good coating effect on $BaTiO_3$. Even when the content of $BaTiO_3$ reached 75 wt%, the composite powder still retained most of the flow characteristics of the PVDF powder. Other flowability parameters of the powder are shown in Fig. S1,† and were in good accordance with the shear test results. From the DSC curves in Fig. 2(e) and (f), the initial melting temperature (T_{im}), initial crystallization temperature (T_{ic}) and sintering window (SW) were obtained and listed in Table 2. The sintering window (SW), representing the region between T_{im} and T_{ic} of the polymer, was the selection range of the preheating temperature. A wide sintering window is beneficial to adjust the SLS processing parameters, effectively avoiding the warpage of the parts. PA11 and PA12 are the most widely used polymer materials for SLS. The sintering windows of PA11 and PA12 are usually in the range of 10–15 °C. The DSC results showed that the sintering windows of PVDF and the PVDF/$BaTiO_3$ powder were always larger than 17 °C, making them suitable for SLS processing.

3.2 The morphology and crystallinity of the PVDF/$BaTiO_3$ SLS parts

The cross sections of the PVDF and composite parts are shown in Fig. 3(a)–(d). With the increase of the $BaTiO_3$ content, the porosity of the SLS parts gradually increased. This was because some of the $BaTiO_3$ particles were exposed on the surface of the powder, which reduced the bonding effect of the powder in SLS processing. When the $BaTiO_3$ content reached 75 wt%, the number of internal structural defects increased greatly. At this time, the tensile strength and elongation at break of the SLS parts were only 2.44 MPa and 0.75%, respectively (Fig. S2†), which could not meet the actual application requirements. The high crystallinity (X_c) and β phase relative amount (K_β) were key to obtaining excellent conversion efficiency. However, different

Table 2 The thermal analysis of PVDF and the PVDF/$BaTiO_3$ powder

Sample	T_{im} (°C)	T_{ic} (°C)	SW (°C)
PVDF	160.7	141.5	19.2
BT25	160.7	142.7	18.0
BT50	160.1	142.9	17.2
BT75	160.5	143.0	17.5

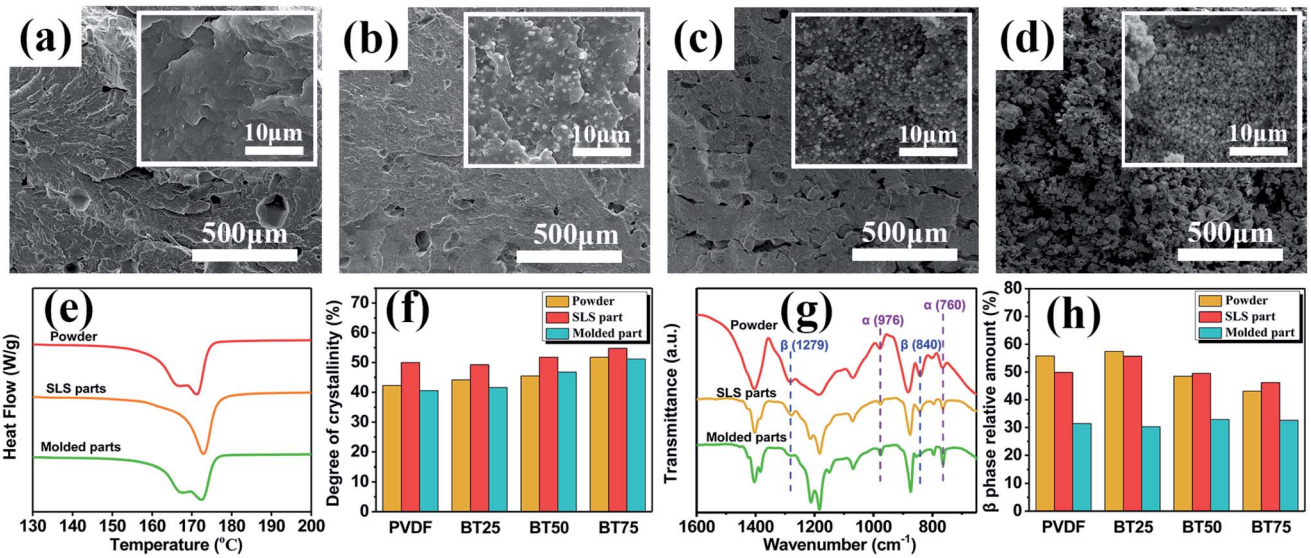

Fig. 3 The SEM images of fractured surfaces of the SLS parts: (a) PVDF, (b) BT25, (c) BT50 and (d) BT75. (e) The DSC curves of the powder, SLS parts and molded parts at the $BaTiO_3$ content of 50 wt%, and (f) the crystallinity of the powder, SLS parts and molded parts. (g) The FT-IR spectra of the powder, SLS parts and molded parts at the $BaTiO_3$ content of 50 wt%, and (h) the β phase relative amount of the powder, SLS parts and molded parts.

from traditional processing methods, SLS processing has a unique way of affecting the crystallization behavior of polymers and the understanding of the related mechanism is not clear enough. For comparison, PVDF/$BaTiO_3$ molded parts were prepared using the SLS powder. The preparation process was as follows: the composite material was first hot pressed at 210 °C for 7 min, then cold pressed at room temperature for 10 min. In order to study the crystallization behavior of the composites during SLS processing, the crystal structures of the powder, SLS parts and molded parts were analyzed by DSC and FT-IR, as shown in Fig. 3(e)–(h). It was clear that due to the imperfect crystal structure in the powder and molded parts, the heating curves both showed double peaks. However, the heating curve of the SLS parts presented a narrow and sharp single peak. The reason was that in SLS processing, the single-layer powder underwent the stage of holding and cooling for several tens of minutes after laser sintering, so the crystal could grow well during this period. In addition, the crystallinity of the SLS parts was significantly higher than that of the powder and molded parts, also illustrating that the crystallization of the SLS parts was more perfect. The FT-IR results showed that the powder, SLS parts and molded parts all exhibited absorption peaks representing α (760 cm^{-1} and 976 cm^{-1}) and β phase (840 cm^{-1} and 1279 cm^{-1}). But different processing methods led to different K_β. The K_β of the SLS parts was close to that of the powder, but much higher than that of the molded parts. This was because the PVDF and PVDF/$BaTiO_3$ powder prepared by this technical route had a relatively high K_β, while the SLS processing only caused partial melting of the powder and was beneficial to the crystallization of PVDF. Therefore, the SLS parts could maintain the crystal structure of the powder to a large extent. In contrast, the powder was completely melted in the molding process and the crystal structure was completely destroyed. Because molding is a processing method with low stress field and it is difficult to induce β phase, the K_β of the molded parts was much lower than that of the powder and SLS parts. In summary, the crystallinity and K_β of the SLS parts both reached about 50%, which was the basis for obtaining excellent piezoelectric properties. It is worth noting that the $BaTiO_3$ content had little effect on the crystallinity and K_β of PVDF and the crystal structure of the composite parts was basically the same with the PVDF parts.

3.3 The crystallization behaviors of the PVDF/$BaTiO_3$ composite powder

In order to further study the crystallization behavior of the powder in SLS processing, the heat transfer process of the powder particles and powder bed under laser irradiation was simulated by the finite element method, and the results are shown in Fig. 4(a)–(e). In the finite element analysis, the heat transfer mode of the "deposited beam power" in the "solid heat transfer" module was adopted. The incident laser power was 10 W. The thermal conductivity of the material was set to 0.2 W $(m\ K)^{-1}$ and the density was 2492 kg m^{-3}, which were derived from the characterization data of the composites. On the one hand, the powder was not completely melted under laser irradiation and the temperature of more than half of the particles was still lower than the melting point (170 °C). So the degree of crystal structure reconstruction after SLS processing was not high. On the other hand, in the process of laser sintering of the powder, the scanning distance between laser beams was 0.1 mm. So there were still some powder particles that were not completely melted, whose crystal structure only changed a little (Fig. 4(d) and (e)). Therefore, the crystal structure of the parts was similar to that of the powder due to the unique processing method of SLS. In order to confirm the experiment and the

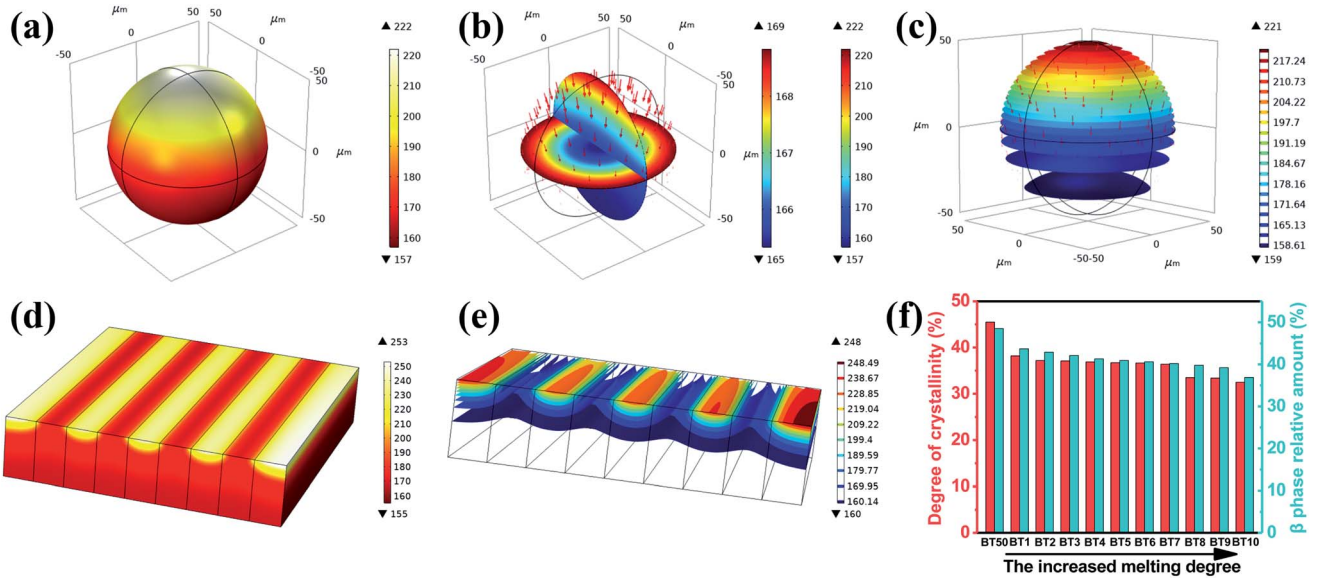

Fig. 4 The finite element analysis of the powder's heat conduction behavior under laser irradiation: (a) surface, (b) section and (c) isothermal surface. The finite element analysis of the powder bed's heat conduction behavior under laser irradiation: (d) surface and (e) isothermal surface. (f) The crystallinity and β phase relative amount of the PVDF/$BaTiO_3$ composites with different melting degrees.

finite element simulation results, the following confirmatory experiments were carried out: the gradual melting of the composites was realized by heating the bottom of the composite powder bed with a certain height. The powder with different heights (*i.e.* different degrees of melting) were characterized by DSC and FT-IR, respectively (Fig. S3†), and the relationship between the crystal structure and the melting degree was established, as shown in Fig. 4(f). Because the powder bed was heated from the bottom, the temperature and the melting degree of the powder increased with the decrease of the height. Meanwhile, the crystallinity and K_β gradually decreased with the increase of the crystal structure reconstruction degree. However, the polymer melt could not be induced to form the polar crystalline phase (β phase) only relying on bottom heating. So the crystallinity and K_β of the composites with a high melting degree were obviously lower than those of the composite powder before melting. Combined with the finite element simulation results, the melting degree of the powder after laser irradiation was closer to that of the upper part of the powder bed in the confirmatory experiment, so the crystallinity and K_β of the SLS parts could reach about 50%, which was similar to that of the powder.

3.4 The piezoelectric performance of the PVDF/$BaTiO_3$ composites and cymbal parts

The frequency-dependent dielectric response of the PVDF and PVDF/$BaTiO_3$ SLS parts is shown in Fig. 5(a). Due to the excellent dielectric properties of $BaTiO_3$, the dielectric constant of the composites increased first and then decreased with the increase of the $BaTiO_3$ content, which was conducive to the improvement of the polarization efficiency and endowed the SLS parts with good piezoelectric properties. Specifically, the dielectric constant of BT50 reached the maximum value of 27.8 at 1000 Hz, which was about 2.7 times than that of PVDF. The ferroelectric *P*–*E* hysteresis curve of BT50 is shown in Fig. S4.† The remnant polarization (P_{ir}) and coercive field (E_{ic}) of BT50 were 70.6 μC m^{-2} and 2.83 kV cm^{-1}, respectively, which exhibited a good polarization effect. However, when the $BaTiO_3$ content was 75 wt%, the dielectric properties of the composites decreased obviously because of a large number of structural defects. The open circuit voltage and short circuit current of the SLS parts under the impact of a linear motor are compared in Fig. 5(b) and (c). The results showed that the piezoelectric properties of the SLS parts also increased first and then decreased with the increase of the $BaTiO_3$ content. When the $BaTiO_3$ content was 50 wt%, the open circuit voltage and short circuit current of the SLS parts reached the maximum, namely 7.3 V and 132.2 nA, respectively. The piezoelectric strain coefficient (d_{33}) of BT50 was 2.0 pC N^{-1}, which was measured by quasi-static d_{33} apparatus (ZJ-3A). Due to the high $BaTiO_3$ content, the bonding effect of the BT75 powder in SLS processing was poor, making it difficult for the BT75 parts to effectively transfer stress and deform. So the piezoelectric performances of the BT75 parts were worse than those of the BT50 parts. In addition, it was gratifying that the piezoelectric properties of the SLS parts were better than those of the molded parts due to the higher β content (Fig. S5†), which proved the great potential of SLS processing in preparing piezoelectric devices. Based on the PVDF/50 wt% $BaTiO_3$ composites, one-piece cymbal structure piezoelectric parts with excellent stress-to-electricity conversion efficiency were prepared by SLS processing. As shown in Fig. 5(d), the cymbal parts were composed of two identical fittings with a cymbal cavity, drawing on the mortise–tenon connection in traditional Chinese carpentry technology, and no adhesive was used. In contrast, the reference parts with the same appearance but without the

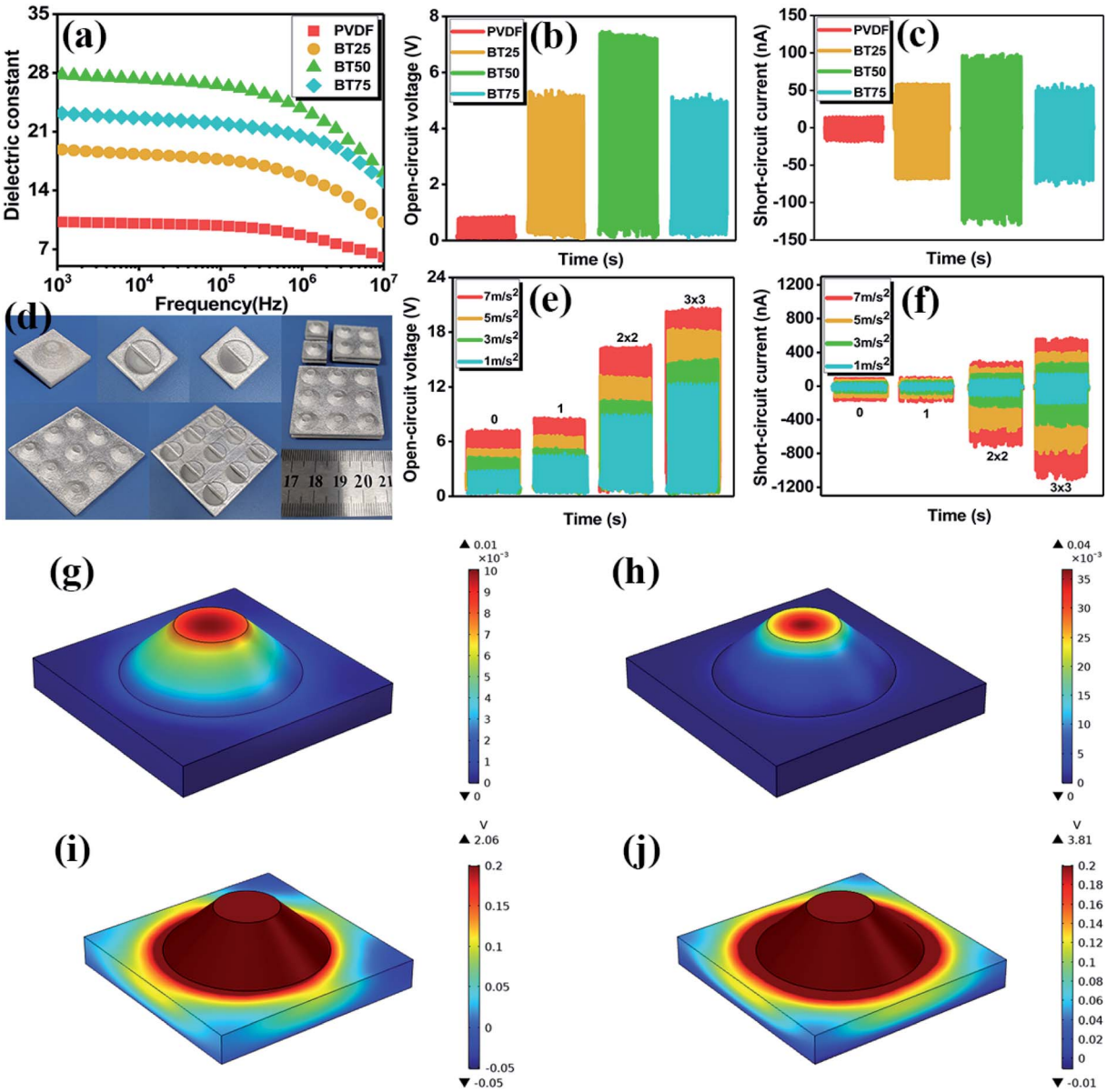

Fig. 5 (a) The frequency-dependent dielectric response, (b) open circuit voltage and (c) short circuit current of the circular SLS parts. (d) Digital photos of the printed cymbal parts. (e) The open circuit voltage and (f) short circuit current generated by the cymbal parts on accelerations ranging from 1 to 7 m s^{-2}. The finite element analysis results: the surface displacement distribution of (g) the reference part and (h) the cymbal part, and the surface electric potential distribution of (i) the reference part and (j) the cymbal part.

cymbal cavity were designed. In order to obtain better piezoelectric properties, the above-mentioned cymbal structure models were connected in series in the form of 2 × 2 and 3 × 3 arrays, respectively. For convenience, the reference parts were named as "0", the cymbal parts as "1", 2 × 2 series connection parts as "2 × 2", and 3 × 3 series connection parts as "3 × 3". The dimensional parameters of the "0", "1", "2 × 2" and "3 × 3" parts were 14 × 14 × 8 mm, 14 × 14 × 8 mm, 28 × 28 × 8 mm and 42 × 42 × 8 mm, respectively. The open circuit voltage and short circuit current of these parts under different acceleration impacts of the linear motor are shown in Fig. 5(e) and (f). Forces of 5.5, 10.0, 15.3 and 24.5 N were applied to the parts subject to impact acceleration rates of 1, 3, 5 and 7 m s^{-2}, respectively. Compared with the reference parts, the cymbal parts were endowed with more excellent piezoelectric properties. This was because the unique cymbal cavity could improve the deformation ability of the parts and effectively transfer the stress. The increased deformation could act on the dipole moments of the composites to promote the separation of the positive and negative charge centers and generate a larger displacement current. In addition, when the external impact changed, the piezoelectric responsiveness of the cymbal parts was better, which was also benefitted from the structural characteristics of the cymbal cavity. The current output and responsiveness of the series connected parts were further enhanced. Under the impact of 7 m s^{-2} acceleration, the open circuit voltage and

short circuit current of the 3 × 3 parts could reach 20 V and 1.1 μA, respectively. In order to quantitatively describe the piezoelectric conversion efficiency, we calculated the output power of the circular parts and cymbal parts under the impact of 5 m s^{-2} acceleration. As shown in Fig. S6,† the output powers of the 2 × 2 and 3 × 3 cymbal parts were significantly higher than those of the circular parts, proving that the design and construction of the cymbal structure could indeed improve the piezoelectric conversion efficiency. The finite element simulation results of the deformation and output voltage generated by the cymbal parts and the reference part under the same external force are shown in Fig. 5(g)–(j). In the finite element analysis, the "solid mechanics" module was adopted. The boundary constraints of the model were carried out according to the actual test conditions and a stress of 10 N was applied to the upper surface. The piezoelectric strain coefficient (d_{33}) of the material was set to 2.0 pC N^{-1}, the density was 2492 kg m^{-3} and the dielectric constant was 28.52, which were derived from the characterization data of the composites. When the cymbal parts were subjected to an external force, they could diffuse the force in time, and prevent stress concentration, promoting a higher response to the external force, and could effectively transform the external force into deformation. In addition, in the process of stress-to-electricity conversion, the cymbal part could produce axial and radial deformation at the same time (Fig. 5(j)), so the piezoelectric coefficients from multiple directions were fully utilized. The excellent piezoelectric output performances of the cymbal parts were the result of the superposition of the piezoelectric properties in the two directions.

The piezoelectric properties of the cymbal parts and other reported parts are compared in Fig. 6. The piezoelectric composites based on PVDF and its modified materials exhibited good conversion efficiency; for example, PVDF/PNM-PT,[46] PVDF-TrFE/$BaTiO_3$,[47,48] PVDF/$BaTiO_3$/AgNWs,[49] PVDF/$NaNbO_3$/RGO,[50] PVDF/MAPbBr,[51] PVDF-TrFE/RGO,[52] PVDF/AgNWs,[53] *etc.* By comparison, the piezoelectric performances of the as-prepared 3 × 3 cymbal parts were further improved, and they had great application prospects in the field of sensing and energy capture.

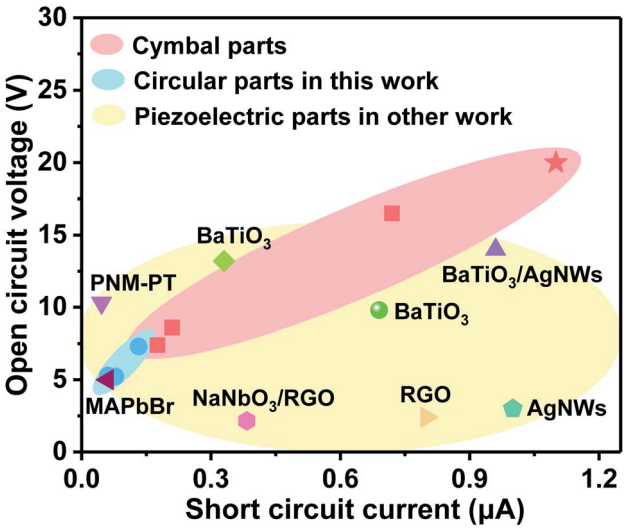

Fig. 6 The comparison of the piezoelectric performance between cymbal structure parts, circular parts and other reported PVDF-based composite parts (the respective composited piezoelectric ceramics are indicated).

4. Conclusions

In summary, a novel PVDF/$BaTiO_3$ piezoelectric composite material suitable for SLS processing was prepared by solid state shear milling technology. High content filled $BaTiO_3$ particles with noble dielectric and piezoelectric properties were evenly dispersed into PVDF *via* the strong shearing force generated from S^3M equipment. The obtained SLS parts were endowed with higher content of electroactivated β phase (up to 56%). What's more, the structurally designed one-piece cymbal part exhibited the performance characteristics of amplifying stress and coupling the piezoelectric coefficients from multiple directions. The open circuit voltage and short circuit current could reach 20 V and 1.1 μA, respectively, which were better than those of the composites reported in other work. This work not only introduced a new manufacturing method for polymer/ceramic piezoelectric composite materials, but also demonstrated a novel piezoelectric performance optimization strategy *via* 3D structural design.

Conflicts of interest

There are no conflicts to declare.

Acknowledgements

This work was kindly supported by the National Natural Science Foundation of China (51933007, 51673123 and 52003174), the National Key R&D Program of China (No. 2017YFE0111500) and the Program for Featured Directions of Engineering Multidisciplines of Sichuan University (No. 2020SCUNG203). We would like to thank the College of Electronics and Information Engineering of Sichuan University for providing COMSOL software.

References

1 R. Lay, G. S. Deijs and J. Malmström, *RSC Adv.*, 2021, **11**, 30657–30673.
2 Z. Duan, Y. Jiang, Q. Huang, S. Wang, Y. Wang, H. Pan, Q. Zhao, G. Xie, X. Du and H. Tai, *Smart Mater. Struct.*, 2021, **30**, 055012.
3 C. Yan, Y. Gao, S. Zhao, S. Zhang, Y. Zhou, W. Deng, Z. Li, G. Jiang, L. Jin, G. Tian, T. Yang, X. Chu, D. Xiong, Z. Wang, Y. Li, W. Yang and J. Chen, *Nano Energy*, 2019, **10**, 104235.
4 X. Zhang, H. Lin, H. Shang, J. Xu and W. Huang, *SusMat*, 2021, **1**, 105–126.
5 D. Zhang, B. Fan, L. Ying, N. Li, C. J. Brabec, F. Huang and Y. Cao, *SusMat*, 2021, **1**, 4–23.
6 N. Sezer and M. Koç, *Nano Energy*, 2021, **80**, 105567.
7 J. Guo, M. Nie and Q. Wang, *RSC Adv.*, 2021, **11**, 1182–1186.

8 Z. Li, G. Zhu, R. Yang, A. C. Wang and Z. L. Wang, *Adv. Mater.*, 2010, **22**, 2534–2537.
9 X. Cheng, X. Xue, Y. Ma, M. Han, W. Zhang, Z. Xu, H. Zhang and H. Zhang, *Nano Energy*, 2016, **22**, 453–460.
10 Q. Zhao, L. Yang, K. Chen, Y. Ma, Q. Peng, H. Ji and J. Qiu, *Compos. Sci. Technol.*, 2020, **199**, 108330.
11 Y. Li, K. Zhang, M. Nie and Q. Wang, *Ind. Eng. Chem. Res.*, 2019, **58**, 22273–22282.
12 X. Liu, Y. Shang, J. Zhang and C. Zhang, *ACS Appl. Mater. Interfaces*, 2021, **13**, 14334–14341.
13 L. Song, R. Dai, Y. Li, Q. Wang and C. Zhang, *ACS Sustainable Chem. Eng.*, 2021, **9**, 7561–7568.
14 H. Cui, R. Hensleigh, D. Yao, D. Maurya, P. Kumar, M. G. Kang, S. Priya and X. Zheng, *Nat. Mater.*, 2019, **18**, 234–241.
15 J. Kim, J. Oh, S. Lim, J. Y. Sim, J. S. Jeon, K. No, S. Park and S. Hong, *Nano Energy*, 2019, **55**, 348–353.
16 C. Yang, N. Chen, X. Liu, Q. Wang and C. Zhang, *RSC Adv.*, 2021, **11**, 20662–20669.
17 C. Shuai, G. Liu, Y. Yang, F. Qi, S. Peng, W. Yang, C. He, G. Wang and G. Qian, *Nano Energy*, 2020, **74**, 104825.
18 L. Song, Z. Huang, S. Guo, Y. Li and Q. Wang, *ACS Appl. Mater. Interfaces*, 2021, **13**, 37252–37261.
19 Y. Jin, N. Chen, Y. Li and Q. Wang, *RSC Adv.*, 2020, **10**, 20405–20413.
20 C. Ribeiro, C. M. Costa, D. M. Correia, J. Nunes-Pereira, J. Oliveira, P. Martins, R. Goncalves, V. F. Cardoso and S. Lanceros-Mendez, *Nat. Protoc.*, 2018, **13**, 681–704.
21 V. S. Bhugra, M. Maddah, G. V. Williams, N. Plank and T. Nann, *RSC Adv.*, 2019, **9**, 31233–31240.
22 P. Li, J. W. Zhai, B. Shen, S. J. Zhang, X. L. Li, F. Y. Zhu and X. M. Zhang, *Adv. Mater.*, 2018, **30**, 1705171.
23 D. Tian, P. Chen, X. Yang and B. Chu, *Ceram. Int.*, 2021, **47**, 17262–17267.
24 C. Yang, S. Song, F. Chen and N. Chen, *ACS Appl. Mater. Interfaces*, 2021, **13**, 41723–41734.
25 S. Song, Y. Li, S. Bai and Q. Wang, *Chem. Eng. J.*, 2021, **415**, 129035.
26 F. Qi, N. Chen and Q. Wang, *Mater. Des.*, 2017, **131**, 135–143.
27 N. Chamankar, R. Khajavi, A. A. Yousefi, A. Rashidi and F. Golestanifard, *Ceram. Int.*, 2020, **46**, 23567–23581.
28 W. Ren, Z. Li, Y. Chen, H. Gao, W. Yang, Y. Wang and Y. Luo, *Macromol. Mater. Eng.*, 2019, **304**, 1800491.
29 P. Eltouby, I. Shyha, C. Li and J. Khaliq, *Ceram. Int.*, 2021, **47**, 17813–17825.
30 S. Yi, W. Zhang, G. Gao, H. Xu and D. Xu, *Ceram. Int.*, 2018, **44**, 10940–10944.
31 S. Yang, W. Li, S. Bai and Q. Wang, *J. Mater. Chem. C*, 2018, **6**, 11209–11218.
32 Y. Li, P. Huang, S. Guo and M. Nie, *J. Cleaner Prod.*, 2020, **272**, 122694.
33 H. Zhang, Y. Zhu and L. Li, *RSC Adv.*, 2020, **10**, 3391–3401.
34 P. Liu, W. Chen, Y. Jia, S. Bai and Q. Wang, *Mater. Des.*, 2017, **134**, 121–131.
35 C. Zhang, Y. Li, W. Kang, X. Liu and Q. Wang, *SusMat*, 2021, **1**, 127–147.
36 Y. Yuan, W. Wu, H. Hu, D. Liu, H. Shen and Z. Wang, *RSC Adv.*, 2021, **11**, 1984–1991.
37 D. Xu, H. Zhang, L. Pu and L. Li, *Compos. Sci. Technol.*, 2020, **192**, 108108.
38 S. Song, Y. Li, Q. Wang and C. Zhang, *Composites, Part A*, 2021, **147**, 106452.
39 Z. Guo, E. Nilsson, M. Rigdahl and B. Hagström, *J. Appl. Polym. Sci.*, 2013, **130**, 2603–2609.
40 W. U. A. Yee, K. Masaya, Y. E. Liu and L. U. Xuehong, *Polymer*, 2007, **48**, 512–521.
41 H. Abdolmaleki and S. Agarwala, *Polymers*, 2020, **12**, 2430.
42 Y. Yang, H. Pan, G. Xie, Y. Jiang, C. Chen, Y. Su, Y. Wang and H. Tai, *Sens. Actuators, A*, 2020, **301**, 111789.
43 J. Jiang, S. Tu, R. Fu, J. Li, F. Hu, B. Yan, Y. Gu and S. Chen, *ACS Appl. Mater. Interfaces*, 2020, **12**, 33989–33998.
44 Z.-z. He, X. Yu, J.-h. Yang, N. Zhang, T. Huang, Y. Wang and Z.-w. Zhou, *Composites, Part A*, 2018, **104**, 89–100.
45 L. Wu, N. Luo, Z. Xie, Y. Liu, F. Chen and Q. Fu, *Compos. Sci. Technol.*, 2020, **190**, 108046.
46 C. Li, P. Hu, H. Meng and Z. Jiang, *J. Solution Chem.*, 2016, **45**, 67–80.
47 S. Siddiqui, D.-I. Kim, L. T. Duy, M. T. Nguyen, S. Muhammad, W.-S. Yoon and N.-E. Lee, *Nano Energy*, 2015, **15**, 177–185.
48 X. Chen, X. Li, J. Shao, N. An, H. Tian, C. Wang, T. Han, L. Wang and B. Lu, *Small*, 2017, **13**, 1604245.
49 B. Dudem, D. H. Kim, L. K. Bharat and J. S. Yu, *Appl. Energy*, 2018, **230**, 865–874.
50 H. H. Singh, S. Singh and N. Khare, *Compos. Sci. Technol.*, 2017, **149**, 127–133.
51 A. Sultana, M. M. Alam, P. Sadhukhan, U. K. Ghorai, S. Das, T. R. Middya and D. Mandal, *Nano Energy*, 2018, **49**, 380–392.
52 R. M. Habibur, U. Yaqoob, S. Muhammad, A. S. M. I. Uddin and H. C. Kim, *Mater. Chem. Phys.*, 2018, **215**, 46–55.
53 D. Mandal, K. Henkel and D. Schmeißer, *Phys. Chem. Chem. Phys.*, 2014, **16**, 10403–10407.